processes

MDPI

Article

Mechanisms and Potential Assessment of CO_2 Sequestration in the Baijiahai Uplift, Junggar Basin

Xiaohui Wang [1], Wen Zhang [1], Qun Wang [1], Kepeng Wang [1], Saisai Qin [1] and Tianyu Wang [2,*]

[1] BGP Inc., CNPC, Zhuozhou 072750, China
[2] National Key Laboratory of Petroleum Resources and Engineering, China University of Petroleum (Beijing), Beijing 102249, China
* Correspondence: wangty@cup.edu.cn

Abstract

To reduce CO_2 emissions, CO_2 geological storage is recognized as an effective approach to decrease atmospheric carbon concentration. Sequestration in deep saline aquifers has become a research focus. However, the physicochemical property changes in saline formations induced by CO_2 injection remain unclear, making it difficult to assess their CO_2 storage potential. This study focuses on saline aquifers within the Jurassic Badaowan formation (J_1b), Sangonghe formation (J_1s), and Cretaceous Tugulu Group (K_1tg) of the Baijiahai Uplift in the Junggar Basin. An integrated methodology combining laboratory experiments—including CO_2 static immersion tests, dynamic displacement tests, X-ray diffraction (XRD), mercury injection capillary pressure (MICP), nuclear magnetic resonance (NMR) measurements, and mechanical testing—with CMG-based numerical modeling was employed to analyze CO_2 storage mechanisms and evaluate storage potential. The results show that after CO_2 immersion, extensive dissolution of calcite in J_1s, clay swelling/cementation in J_1b, and extensive dissolution of calcite in K_1tg all lead to increased porosity and permeability, with the J_1b formation exhibiting superior CO_2 storage capacity, the highest MICP-derived porosity, and the greatest NMR-measured porosity among the three formations. Numerical simulations further confirmed J_1b's leading sequestration volume. Based on integrated experimental and simulation results, the J_1b formation is identified as the optimal reservoir for CO_2 storage. However, to manage potential mechanical instability during real-world injection scenarios, injection pressures and rates should be carefully controlled and continuously monitored to avoid formation fracturing and ensure long-term storage security. This study provides a reference for implementing saline aquifer CCUS projects.

Keywords: CO_2 geological storage; Baijiahai uplift; storage potential; storage mechanism; numerical simulation

check for updates

Academic Editor: Qingbang Meng

Received: 24 June 2025
Revised: 14 July 2025
Accepted: 11 August 2025
Published: 21 August 2025

Citation: Wang, X.; Zhang, W.; Wang, Q.; Wang, K.; Qin, S.; Wang, T. Mechanisms and Potential Assessment of CO_2 Sequestration in the Baijiahai Uplift, Junggar Basin. *Processes* **2025**, *13*, 2648. https://doi.org/10.3390/pr13082648

Copyright: © 2025 by the authors. Licensee MDPI, Basel, Switzerland. This article is an open access article distributed under the terms and conditions of the Creative Commons Attribution (CC BY) license (https://creativecommons.org/licenses/by/4.0/).

1. Introduction

Under the severe circumstances of global climate change, environmental issues caused by CO_2 emissions pose a common challenge for countries to maintain sustainable development [1–3]. According to statistics from the International Energy Agency (IEA) [4], global CO_2 emissions reached 36.8 billion tons in 2023, an increase of approximately 18% compared to 2010, and nearly 50% higher than at the beginning of the Industrial Revolution [5,6]. To mitigate the impacts of climate change [7], reducing atmospheric CO_2 concentration has become a key initiative. As a critical component of carbon capture, utilization, and storage (CCUS) technologies [8], CO_2 storage has been proven economically feasible [9] and

its environmental risks predictable [10]. Among various approaches, deep saline aquifer geological CO_2 storage has attracted significant attention due to its wide distribution and enormous storage potential [11–13]. Saline aquifers, typically located in deep sedimentary basins, are characterized by large thickness, moderate porosity and permeability, and stable distribution, providing ideal storage spaces for CO_2 and being regarded as the most promising storage formations [8,14,15].

The storage mechanisms of CO_2 in saline aquifers mainly include physical storage (structural storage and residual gas storage) [16,17] and chemical storage (dissolution storage and mineral storage); physical storage can accommodate large amounts of CO_2 but is unstable, as the trapped CO_2 is vulnerable to leakage due to tectonic movements such as faults and fractures [18,19]; chemical storage offers stronger stability but acts over relatively longer timescales [20,21]. However, the migration patterns of CO_2 in saline aquifers remain incompletely understood. Complex geological structures and fluid properties affect CO_2 distribution and diffusion, making it difficult to accurately predict its long-term storage behavior. The sealing integrity of caprocks is critical for storage safety, yet how to evaluate their ability to resist CO_2 leakage under long-term geological conditions requires further study. Additionally, the chemical reaction rates between CO_2, saline water, and formation minerals are slow, meaning physical storage dominates in the short term, while the effects and influencing factors of long-term chemical storage still need further exploration.

Previous studies have addressed various aspects of CO_2 storage in saline aquifers. Li et al. [22] investigated the distribution and geological characteristics of potential CO_2 reservoirs in deep saline aquifers of the Bohai Bay Basin. Zhao Yulong et al. [21] evaluated the CO_2 storage potential in saline aquifers and developed an adaptive evaluation method to better understand CO_2 migration characteristics. Gholami et al. [23] found that injected CO_2 further migrates and accumulates in pore throats under resistance, reducing reservoir porosity and permeability. Edem et al. [24] conducted core flooding experiments on Gray Berea sandstone with different salinities (5, 15, 25 wt.% NaCl) and found that permeability increased from 10% to 70%, and porosity increased from 0.75% to 6% with increasing salinity. Jia Haizheng et al. [25] investigated the interactions between CO_2 and Jimusaer reservoir rocks, revealing differences in CO_2 storage capacity among different rock types. Mohd Amin et al. [26] observed that porosity decreased most significantly at the interface between reservoir and caprock due to mineral precipitation, enhancing the caprock sealing capacity in the presence of mineral precipitation. Alzayer et al. [27] modeled CO_2 storage in deep saline aquifers and studied best practices for simulating CO_2 storage in deep brine-bearing layers. Ji Youjun et al. [28] investigated the effects of CO_2 geological storage on reservoir mechanical properties and gas migration—diffusion under multi-field coupling through stress sensitivity experiments and numerical simulations. Yiyang Zhou et al. [29] studied CO_2 storage effects in deep saline aquifers under different phases through relative permeability tests and numerical simulations. Peng Xiyi et al. [30] analyzed the influence of CO_2 behavior differences (liquid vs. supercritical states) on plume dynamics evolution through migration experiments in saline aquifers. Fatima et al. [31] investigated the impacts of CO_2 storage on geomechanical and petrophysical properties under different caprock conditions using laboratory experiments and numerical simulations with CMG software 2023.10. Jin Yangjun et al. [32] studied the variation in CO_2 solubility in deep saline aquifers with burial depth through numerical simulations. Temitope et al. [33] used CMG to simulate the feasibility of commercial CO_2 injection in saline aquifers in the United Arab Emirates, revealing CO_2 migration pathways into the aquifers.

Despite these achievements, research on the Baijiahai Uplift in the Junggar Basin remains insufficient. Existing studies lack systematic insights into mineral reactions between CO_2 and local formation minerals, as well as changes in reservoir physical properties before

and after CO_2 exposure in this region's saline aquifers. In terms of storage potential evaluation, precise assessment models tailored to the unique geological conditions of the Baijiahai Uplift have not been established, and some geological parameters are obtained inaccurately or incompletely. Additionally, potential environmental impacts arising during long-term CO_2 storage remain underexplored. Addressing these gaps, this study focuses on the saline aquifers of the Baijiahai Uplift, using a combination of physical experiments and numerical simulations to perform the following: (1) Clarify reservoir physical properties and mineral reactions before and after CO_2 exposure. (2) Establish an appropriate evaluation model for CO_2 storage potential in the region's saline aquifers, calculate CO_2 storage capacity, and assess storage potential. (3) Identify CO_2 storage mechanisms and key controlling factors. (4) Optimize the selection of the best CO_2 storage formation in the Baijiahai area.

2. Research Area

As illustrated in Figure 1, the Baijiahai area in the Junggar Basin of Xinjiang, China, presents an ideal reservoir for carbon capture, utilization, and storage (CCUS) technology. This suitability stems from its combined advantages in geological structure, reservoir characteristics, and existing oil and gas development infrastructure.

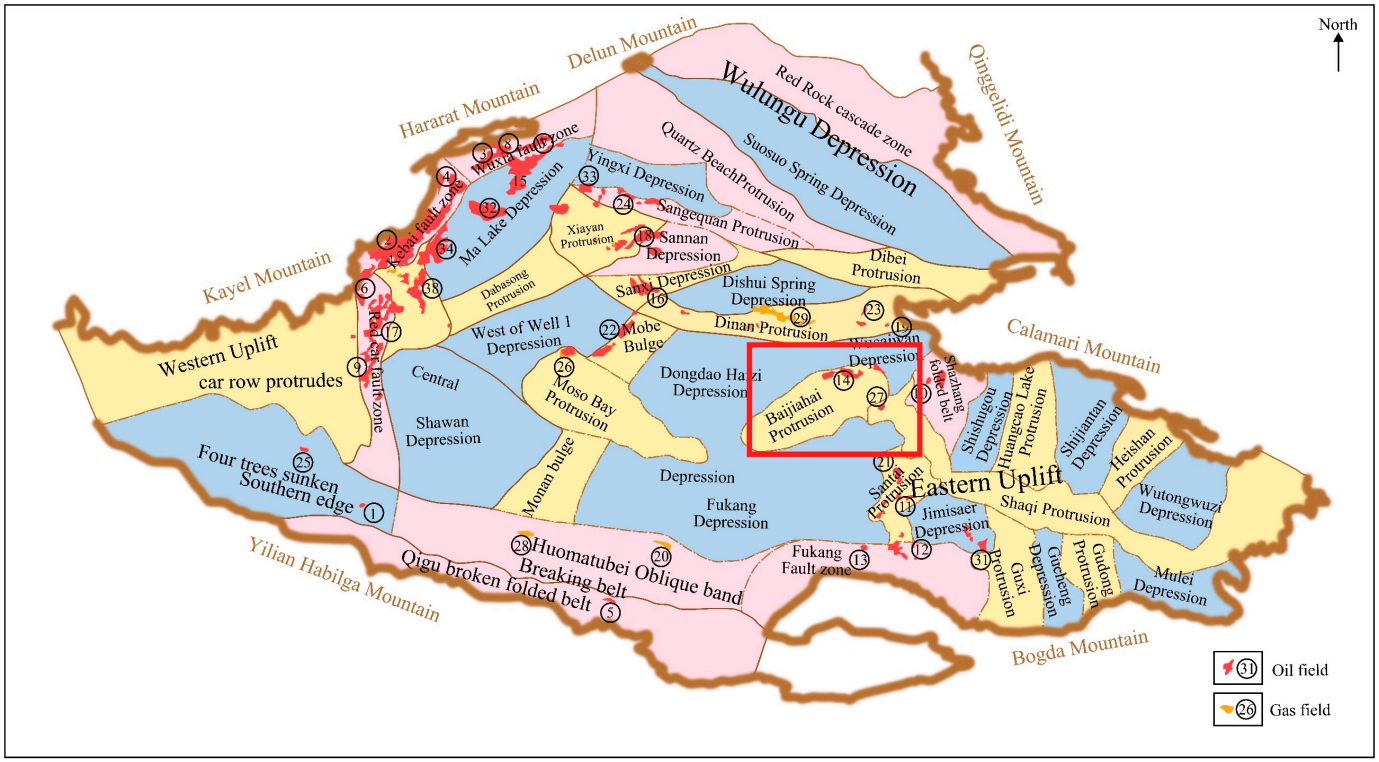

Figure 1. Location of the Baijiahai Uplift area.

This study involved sampling, experimental work, and numerical simulations targeting three geological formations: the Jurassic Badaowan formation (J_1b), Sangonghe formation (J_1s), and Cretaceous Tugulu Group (K_1tg). An offline (ex situ) dry measurement method based on the interaction of X-rays with solid matter was employed [34]. Three representative rock samples were selected from each formation for whole-rock and clay mineral composition analysis, with their average values taken as the typical mineral composition of the formation, as shown in Figure 2. The analysis revealed that the J_1b formation is rich in quartz and clay minerals, with quartz accounting for 53.1%, clay minerals for 25.2%, plagioclase for 14.7%, and potassium feldspar for 6.8%, among which kaolinite is the main clay mineral. The J_1s formation is mainly composed of quartz and plagioclase,

with quartz content of 56.9%, plagioclase of 24.1%, potassium feldspar of 8.1%, and clay minerals of 10.9%, including kaolinite, illite–montmorillonite mixed layers, and chlorite. The K_1tg formation is rich in calcite and quartz, with a calcite content of 42.6%, quartz of 22.3%, plagioclase of 14.8%, potassium feldspar of 5.7%, and clay minerals of 13.8%, with illite–montmorillonite mixed layers as the main clay minerals.

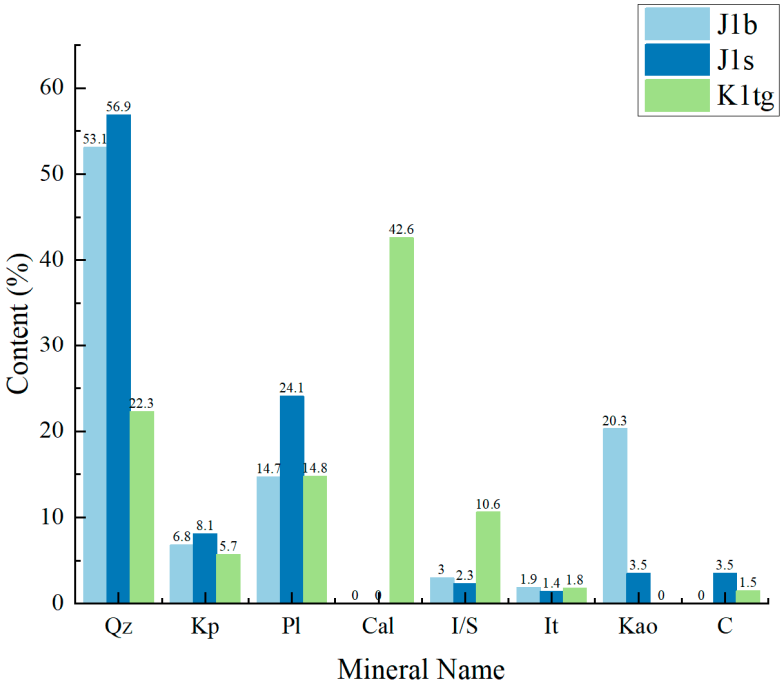

Figure 2. Mineral composition and corresponding contents of the 3 formations.

3. Research Method

3.1. Technical Roadmap

This study employs an integrated methodology combining laboratory experiments and numerical simulations, grounded in seepage mechanics, geochemistry, and multiphysics coupling theory, to investigate gas–water–rock interactions during CO_2 injection in the Baijiahai area reservoirs. Physical simulation experiments and reaction mechanisms are examined through this approach, with the technical roadmap detailed in Figure 3.

3.2. Sample Preparation

Core samples were taken from Well Shaqiu-3, Shaqiu-101, Shaqiu-103, Cai-002, and Cai-10 (K_1tg, J_1b, J_1s formations), as shown in Figure 4. Formation water was prepared at a concentration of 12 g/L of KCl and 300 mg/L of Na_2CO_3, and an experimental plan was developed. The parameters set for each test are listed in Table 1.

3.3. CO_2 Immersion and Displacement Experiments

To simulate the interaction between supercritical carbon dioxide (SC-CO_2) and formation rock samples from J_1s, J_1b, and K_1tg under reservoir conditions, self-developed high-temperature and high-pressure immersion experimental equipment was used to carry out SC-CO_2 + formation water coupling immersion experiments. The specific procedure is as follows: First, place the rock samples in the glass container shown in Figure 5c, inject formation water, and perform vacuum saturation treatment. Remove the samples after 4–5 h. Then transfer the formation water-saturated rock samples to the intermediate container shown in Figure 5a (adopting a 316 L stainless steel piston structure with a volume of 500 mL, pressure resistance of 70 MPa, and equipped with a fluor rubber sealing ring).

Supply gas from the CO_2 gas cylinder in Figure 5b and conduct immersion experiments at a constant temperature of 40 °C for different durations. After the experiments, remove the samples and dry them in an oven at 85 °C for 12 h.

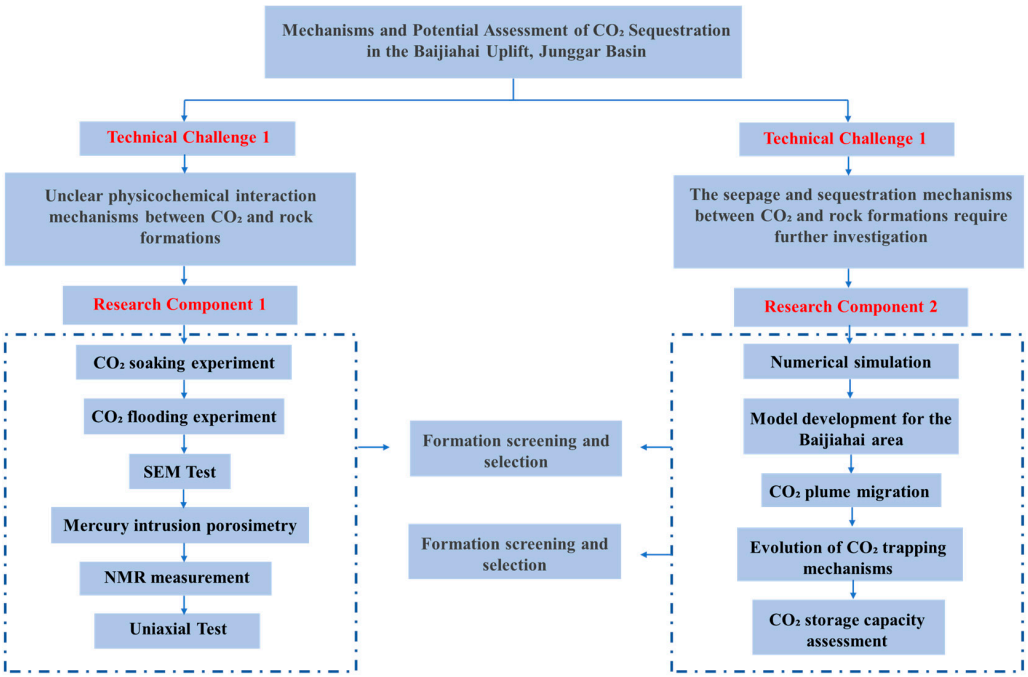

Figure 3. Technical workflow.



Figure 4. Core sampling.

Table 1. Settings of test parameters for each experiment.

Test	Formation	CO_2 Immersion Time	CO_2 Immersion Temperature
Mercury Injection Test	J_1s J_1b K_1tg	24 h	40 °C
SEM Test	J_1s J_1b K_1tg	24 h	40 °C
Uniaxial Compression Test	J_1s J_1b K_1tg	24 h	40 °C
Uniaxial Shear Test	J_1s J_1b K_1tg	24 h, 48 h, 60 h 24 h, 48 h, 60 h 24 h, 48 h, 60 h	40 °C 40 °C 40 °C

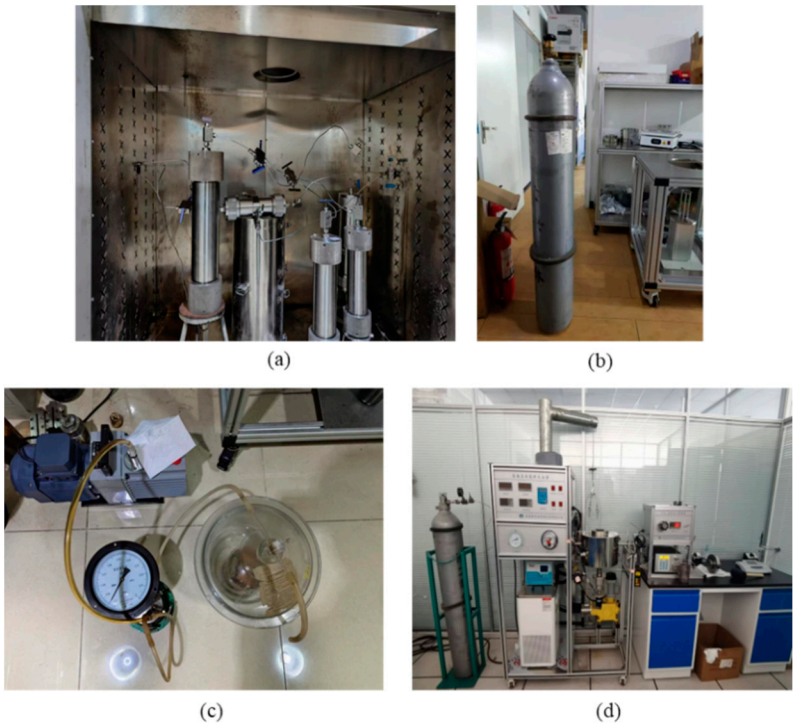

Figure 5. (**a**) Intermediate container for CO_2, (**b**) CO_2 gas cylinder, (**c**) glass container, and (**d**) displacement experiment device.

Displacement experiments were used to evaluate the CO_2 storage capacity of the 3 formations. In the experiments, the displacement parameters for J_1s rock samples were set as follows: injection pressure of 12 MPa, confining pressure of 14 MPa, outlet pressure of 11.5 MPa, and temperature of 40 °C. For J_1b and K_1tg rock samples, a parameter combination of an injection pressure of 24 MPa, confining pressure of 26 MPa, outlet pressure of 23.5 MPa, and temperature of 40 °C was adopted, and the experiments were carried out using a displacement holder equipped with a back-pressure regulator (in Figure 5d). The experimental steps include the following: First, saturating the rock samples with formation water; second, measuring the porosity and wet weight of the saturated rock samples; finally, displacing with CO_2 and recording the changes in porosity and weight after displacement.

3.4. MICP, NMR, and Mechanical Testing

Mercury intrusion testing provides fundamental pore-throat structure data for analyzing reservoir storage capacity and studying CO_2 migration patterns. During the test, samples before and after immersion are fixed by a holder, and the American Micromeritics AutoPore IV-9500 fully automated mercury porosimeter (as shown in Figure 6b) is used. The displacement pressure range is set to 0.014–0.301 MPa. The uncertainties in MICP interpretation primarily arise from the following aspects: contact angle, mercury wettability, pore connectivity, compression effects, sample representativeness, and hysteresis effects. To mitigate these uncertainties, we have adopted standardized procedures by implementing the National Standards of the People's Republic of China—GB/T 29172-2012 [35] "Core Analysis Methods" and GB/T 29171-2012 "Determination of Rock Capillary Pressure Curves". This ensures relatively consistent experimental conditions and reduces errors. Additionally, we alleviate these uncertainties through replicate experiments and maintaining consistency throughout the entire pre-treatment process.



(a) (b) (c)

Figure 6. (**a**) NMR instrument, (**b**) Micromeritics AutoPore IV-9500 Mercury Intrusion Porosimeter, and (**c**) TAR-1500 high-temperature and high-pressure rock rheometer.

NMR testing is conducted using the NMRC12-010V Cryogenic Nano-Porosity Analyzer and Supra22k Centrifuge, designed and constructed by SuZhou Niumag Analytcal instrument Corporation (Suzhou, China). It provides a comprehensive characterization of reservoir pore structure and pore size distribution, offering essential technical support for optimizing CO_2 injection strategies. The procedure is as follows: The core is first cleaned to remove residual oil, then dried in an oven for 24 h until a constant weight is achieved. Its dry weight, length, and diameter are recorded. The core is subsequently vacuum-saturated with formation water for more than 4 h and weighed again to obtain its wet weight. NMR T_2 spectrum measurements are conducted using the equipment shown in Figure 6a. Following the displacement experiment, a second NMR T_2 spectrum test is performed. By comparing the T_2 spectra before and after displacement, the T_2 cutoff value for movable fluids can be determined.

Mechanical testing serves as a critical tool for assessing reservoir stability. Determining the mechanical strength and deformation behavior of reservoir rocks enables an evaluation of the risks associated with fracture initiation, deformation, subsidence, and stress sensitivity following CO_2 injection. These assessments provide essential evidence for evaluating the safety and long-term effectiveness of geological CO_2 storage. In this study, triaxial mechanical tests were conducted on samples before and after CO_2 exposure using the hydraulic servo testing system TAR-1500, designed and constructed by Changchun Huiyang Co. Ltd. (Changchun, China) as shown in Figure 6c, including uniaxial tensile and shear strength tests, to systematically investigate the mechanical response of the reservoir rocks under simulated subsurface conditions.

4. Experimental Results

4.1. NMR Tests Before and After Displacement

4.1.1. Nuclear Magnetic Resonance Results

Figures 7–9 present the nuclear magnetic resonance (NMR) T_2 spectrum curves of the J_1s, J_1b, and K_1tg formations, respectively, measured before and after 24 h of CO_2 displacement. By analyzing the morphological evolution of the T_2 spectra, the shifts in characteristic peaks, and the differences in cumulative porosity pre- and post-displacement, the influence of CO_2 injection on pore structure—including pore size distribution and connectivity—as well as fluid occurrence states, was quantitatively characterized. The extent of porosity reduction directly reflects the storage effect, offering an intuitive measure of CO_2 sequestration efficiency. These analyses provide critical multi-scale insights into the CO_2–brine–rock interaction mechanisms and highlight formation-specific differences in storage performance. The detailed interpretation is as follows:

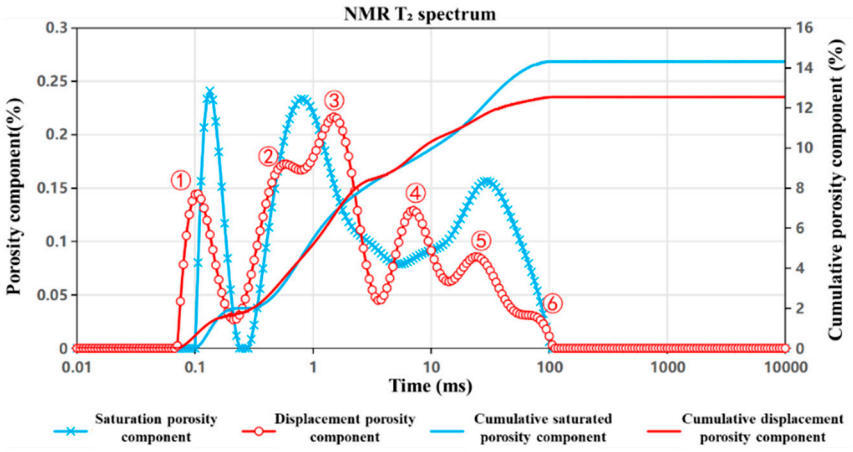

Figure 7. NMR T_2 spectrum curve of the J_1s formation.

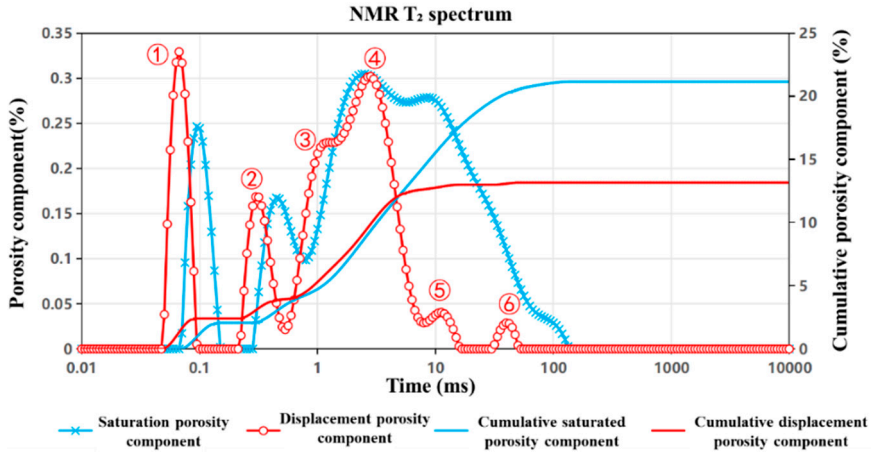

Figure 8. NMR T_2 spectrum curve of the J_1b formation.

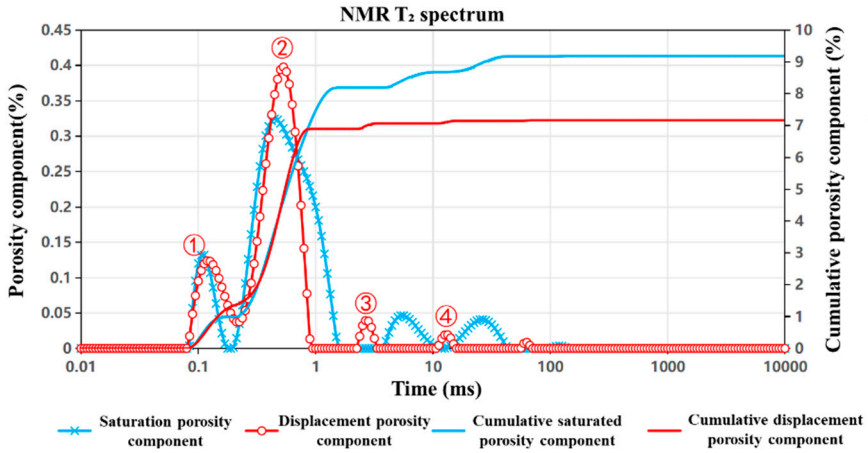

Figure 9. NMR T_2 spectrum curve of the K_1tg formation.

For the J_1s formation (Figure 7), the T_2 distribution curve (red) shifts toward the intermediate relaxation time region following displacement, indicating a trend toward pore structure homogenization. This suggests that the displacement process enhances the uniformity of pore size distribution and improves overall fluid connectivity. NMR measurements yield a T_2 cutoff value of 53.6 ms. Porosity decreases slightly from 14.3% prior to displacement to 13.1% afterward, with a cumulative porosity separation of 1.2%, reflecting a modest CO_2 storage effect. Characteristic peak analysis reveals the following:

(1) Within the 0.1–1 ms interval, both the number and size of Peak ① (small pores) decrease.
(2) Peak ② (small-to-medium pores) shows a reduction in number but an increase in size.
(3) In the 1–10 ms interval, Peaks ③ and ④ (medium pores) display a significant increase in number.
(4) In the 10–100 ms range, Peak ⑤ (medium-to-large pores) decreases in number while its size remains largely unchanged, and Peak ⑥ (large pores) exhibits an increase in pore size.

The mineralogical composition of the J_1s formation is dominated by silicates, which are chemically stable and exhibit minimal reactivity with the acidic environment generated by CO_2–brine interaction. As a result, the displacement process primarily affects the movable fluid (brine) within pre-existing large pore channels. Minor enhancements in connectivity are observed in microfractures and smaller pores, contributing to a more uniform pore network, with only limited reductions in overall movable porosity.

These results suggest that CO_2 injection in the J_1s formation induces a redistribution of pore fluids and a moderate reorganization of the pore structure. The observed increase in medium-pore content and the homogenization of the pore system may enhance short-term injectivity and fluid mobility. However, due to the relatively small increase in cumulative porosity and the reduction in small-pore volume, the formation's long-term CO_2 storage capacity remains limited.

For the J_1b formation (Figure 8), the T_2 distribution curve (red) exhibits a distinct shift toward the shorter relaxation time region (<1 ms) following displacement, with residual signal intensity concentrated within the ultra-small-pore domain. This shift reflects a notable increase in the abundance of micropores and an overall reduction in effective pore size, accompanied by the structural reconfiguration of previously dominant macropore networks. NMR measurements reveal a T_2 cutoff value of 58.9 ms, with porosity declining markedly from 21.2% pre-displacement to 12.8% post-displacement. The cumulative porosity separation difference reaches 8.4%, representing the highest among all tested formations and suggesting a pronounced CO_2 trapping capacity. Detailed T_2 spectral analysis indicates the following trends:

(1) In the 0.01–1 ms range, the intensity of Peak ① (small pores) increases, though the corresponding pore sizes diminish.
(2) Peak ② (small-to-medium pores) retains a stable amplitude while shifting toward smaller sizes.
(3) Within the 1–10 ms range, Peak ③ (small-to-medium pores) exhibits increased amplitude, while Peak ④ (medium pores) remains largely unchanged in both size and number.
(4) In the 10–100 ms range, Peak ⑤ (medium-to-large pores)—representing the principal pore-throat domain for CO_2 storage—undergoes a significant decline in amplitude with stable size, whereas Peak ⑥ (large pores) shows a slight increase in pore size.

The elevated clay mineral content of the J_1b formation plays a pivotal role in this pore structure evolution. Under acidic CO_2–brine conditions, clay minerals are prone to swelling, exfoliation, or precipitation, which may partially obstruct macropores. Simultaneously, the disaggregation of clay aggregates can generate a substantial number of micro- and nano-scale pores and microfractures. These processes, coupled with clay particle migration and secondary cementation, result in the reconfiguration of original intergranular pores and fractures, promoting a transition from macroporous to microporous systems. Consequently, bound water becomes the dominant fluid phase post-displacement.

Collectively, the NMR results indicate that CO_2 injection induces a substantial redistribution of pore size within the J_1b formation, characterized by a marked increase in

micropore populations and the restructuring of macropore pathways. The significant cumulative porosity separation (8.4%) underscores the superior CO_2 sequestration potential of the J_1b formation, primarily through enhanced capillary trapping facilitated by newly generated microporous structures.

For the K_1tg formation (Figure 9), the T_2 distribution curve (red) concentrates around Peak ② (representing small-to-medium pores) after displacement, indicating that the displacement process primarily affects large pores, while bound water in smaller pores remains relatively unchanged. NMR testing shows that porosity decreases from 9.2% before displacement to 7.2% after displacement, with a cumulative porosity separation difference of 2%, suggesting a moderate CO_2 storage effect. Characteristic peak analysis reveals the following:

(1) In the 0.01–1 ms range, there is no significant change in Peak ① (small pores).
(2) The number of Peak ② (small-to-medium pores) increases, although their size remains constant.
(3) In the 1–10 ms range, the amplitude of Peak ③ (medium pores) decreases.
(4) In the 10–100 ms range, both the amplitude and size of Peak ④ (large pores) decrease.

These findings confirm that CO_2 injection predominantly displaces fluids in larger pores, while smaller pores retain their bound water content.

In K_1tg, calcite is easily dissolved by acidic CO_2–water, forming new mesopores approximately 1 μm in size, leading to an increase in the peak area within the 0.1–1 ms interval. Meanwhile, fluids in larger pores (10–100 ms interval) are preferentially displaced, causing a decrease in this peak. However, due to the structural stability of the carbonate framework, some large pores are still preserved.

4.1.2. Displacement Results

Through displacement experiments, the process of supercritical CO_2 injection into saline aquifers under realistic geological conditions was simulated. By precisely measuring the mass of rock samples in key states—dry, saturated with formation water, and after CO_2 displacement—the amount of CO_2 stored in formation pore spaces (by displacing pore water and occupying its volume) was directly and quantitatively calculated. This approach provides the most direct experimental evidence for evaluating the actual storage capacity of different reservoirs. The experimental results are as follows:

The dry mass of the J_1s sample was 52.9 g, which increased to 56.51 g after saturation with formation water, and decreased to 56.04 g after CO_2 displacement, indicating a CO_2 storage amount of 0.47 g. The J_1b sample had a dry mass of 51.1 g, a saturated mass of 56.44 g, and a post-displacement mass of 53.98 g, corresponding to a CO_2 storage amount of 2.46 g. The K_1tg sample had a dry mass of 60.5 g, increased to 62.8 g after saturation, and decreased to 62.08 g after displacement, resulting in a CO_2 storage amount of 0.72 g.

These results clearly demonstrate that the J_1b formation sample exhibits the highest CO_2 storage capacity among the formations tested.

4.2. Mercury Injection Test

Displacement experiments simulate the actual migration process of CO_2 in reservoirs, enabling the quantification of CO_2 storage capacities in different formations and revealing the dynamic interaction mechanisms between CO_2, formation fluids, and rock pore structures. The results form a closed-loop data system with mercury intrusion testing and NMR testing—changes in pore-throat radius reflected by capillary pressure curves (e.g., the maximum pore-throat radius of J_1s increasing from 25 μm to 40 μm) directly explain the phenomenon of permeability leap after displacement (from 204.1 mD to 1665.5 mD), while improvements in pore-throat sorting (e.g., the median pore-throat radius of J_1b in-

creasing from 0.183 μm to 0.406 μm) and post-displacement porosity changes (e.g., J_1b decreasing from 21.2% to 12.8%) jointly confirm the contributions of capillary trapping and mineral reactions to storage efficiency. Additionally, the T_2 cutoff value of movable fluids recorded in displacement experiments (e.g., 53.6 ms for J_1s), combined with mercury intrusion saturation from capillary pressure curves (e.g., J_1s increasing from 91.85% to 92.78%), further quantifies the occurrence states of CO_2 in different pore size intervals, providing critical measured data for parameter calibration in multi-field coupling models of numerical simulations. The results of mercury intrusion experiments are as follows:

After a 24 h immersion at 40 °C, in Figure 10, the permeability of J_1s increased from 204.1 mD to 1665.5 mD, porosity rose from 20.8% to 21.5%, the median pore-throat radius increased from 2.214 μm to 5.757 μm, and the maximum mercury saturation increased from 91.85% to 92.78%. With permeability enhanced by over seven times and a 160% increase in the median pore-throat radius, the results indicate significant enlargement of throat sizes and greatly improved seepage capacity after immersion. However, the low overall porosity and extremely small median pore-throat radius limit its suitability as an optimal reservoir for CCUS applications.

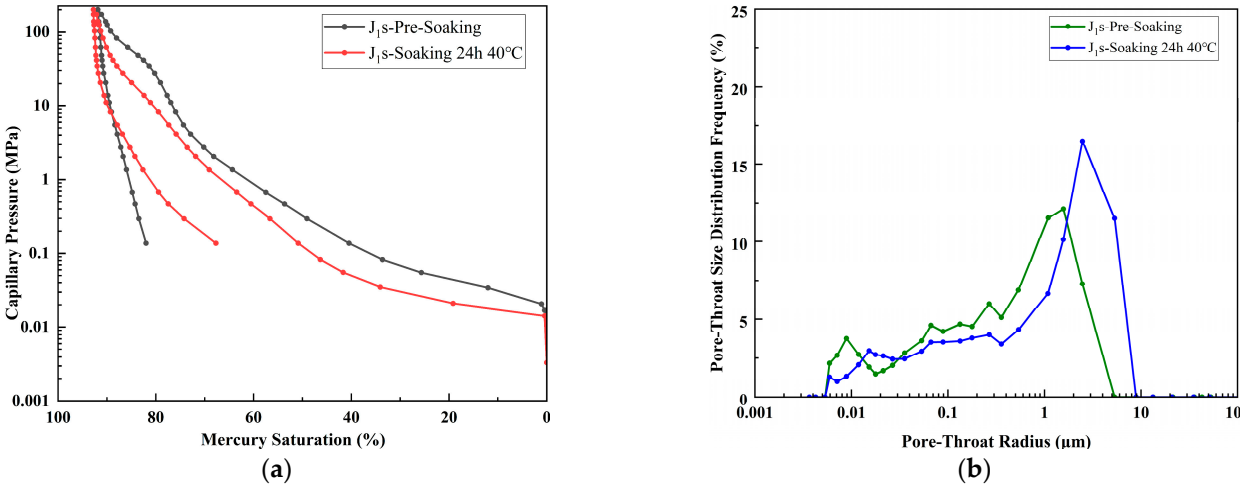

Figure 10. (**a**) Capillary pressure curves of sample J_1s prior to immersion and following 24 h immersion at 40 °C. (**b**) Pore size distribution curves of sample J_1s prior to immersion and following 24 h immersion at 40 °C.

For J_1b in Figure 11, immersion at 40 °C for 24 h caused permeability to increase from 13.140 mD to 110.757 mD, porosity to rise from 26.559% to 29.947%, the median pore-throat radius to increase from 0.183 μm to 0.406 μm, and the maximum mercury saturation to increase from 87.437% to 90.323%. The enlarged pore-throat radius, improved sorting, and enhanced connectivity—with the pore-throat radius doubled—confirm the development of microfractures or dissolution of clay minerals, which significantly eliminated seepage bottlenecks and caused a 743% surge in permeability. These changes marked an enlargement of pore throats, improved sorting, and enhanced connectivity, confirming the development of microfractures and/or the dissolution of clay minerals, effectively removing seepage bottlenecks. Such physicochemical modifications significantly boost the seepage capacity and suggest greatly improved injectivity and storage performance for CO_2 sequestration in the J_1b reservoir.

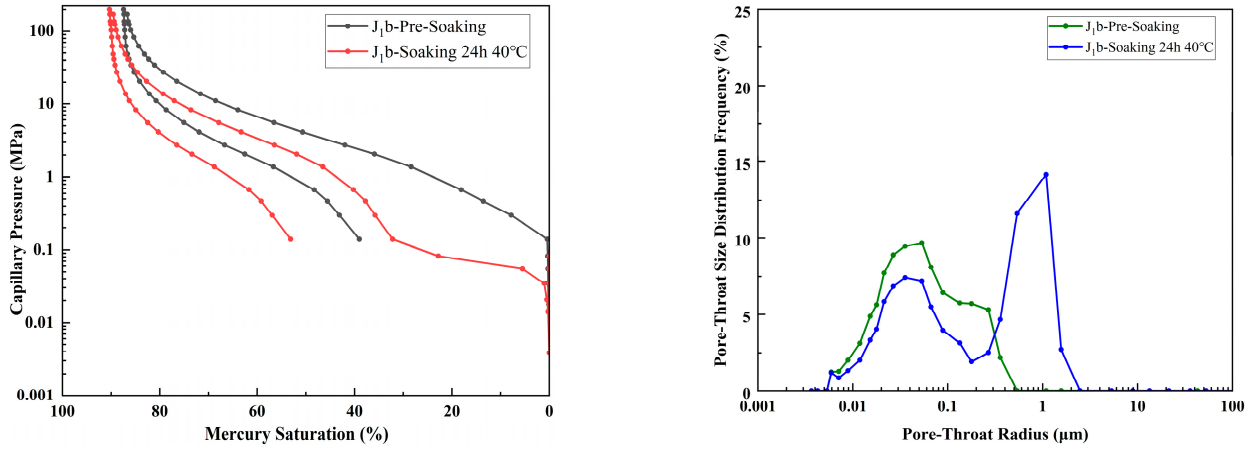

Figure 11. (**a**) Capillary pressure curves of sample J_1b prior to immersion and following 24 h immersion at 40 °C. (**b**) Pore size distribution curves of sample J_1b prior to immersion and following 24 h immersion at 40 °C.

For K_1tg in Figure 12, immersion at 40 °C for 24 h led to an increase in permeability from 3.901 mD to 7.777 mD, porosity from 21.486% to 23.429%, the median pore-throat radius from 0.058 μm to 0.159 μm, and the maximum mercury saturation from 85.971% to 88.039%. Despite a 174% increase in the pore-throat radius, the absolute value of 0.159 μm remained extremely small, resulting in slow permeability growth and moderate mercury saturation changes, with pore enlargement primarily occurring in small-to-medium pores. However, the absolute throat size remains very small, so permeability enhancement is limited, and pore accessibility improvements are modest. The mechanical properties are relatively stable.

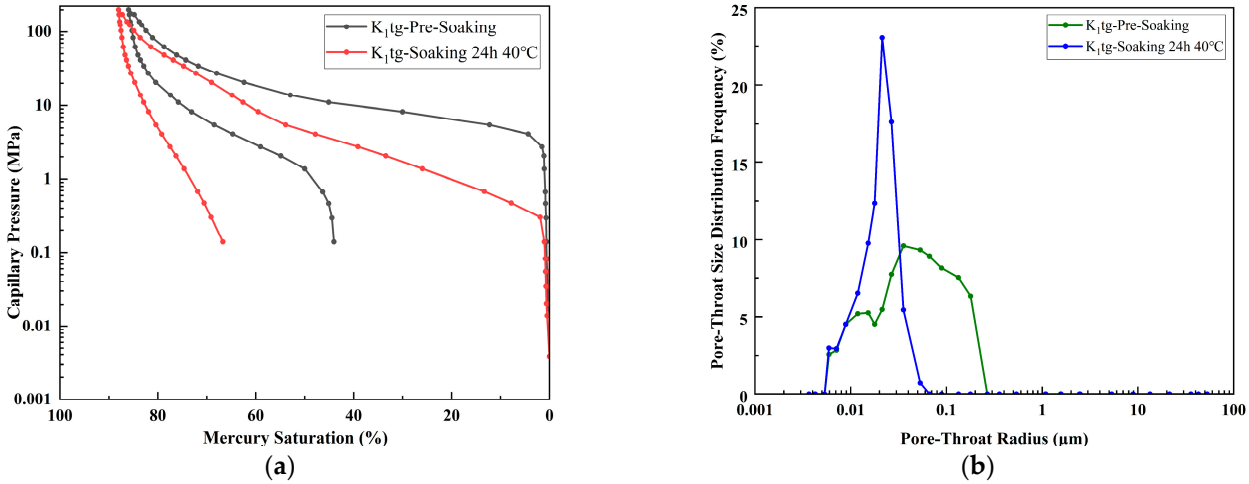

Figure 12. (**a**) Capillary pressure curves of sample K_1tg prior to immersion and following 24 h immersion at 40 °C. (**b**) Pore size distribution curves of sample K_1tg prior to immersion and following 24 h immersion at 40 °C.

4.3. The Evolution Law of Mechanical Characteristics

Stress–strain curves of J_1s, J_1b, and K_1tg formations obtained from uniaxial compressive tests after CO_2 immersion for 24 h and 48 h at 40 °C are shown in Figures 13 and 14. The results indicate that as the CO_2 immersion time extends from 24 h to 48 h, the curves shift entirely toward the low-stress region, with the strain-softening stage prolonged and its shape tending to flatten. Specifically, the peak stress decreases, reflecting the decay of the

rock samples' compressive strength; the residual strain increases, indicating a significant enhancement in plastic deformation capacity. This phenomenon reveals the time-dependent degradation effect of CO_2–water–rock interaction on the mechanical properties of reservoir rocks. Regarding wellbore stability, the shear strength of the J_1s formation plummets by 20.57% within 24 to 48 h, making the cement sheath highly susceptible to early-stage shear failure and increasing the risk of annular channeling. The J_1b formation exhibits delayed deterioration, with a 10.95% reduction in shear strength between 48 and 60 h. Long-term CO_2 penetration may dissolve cementitious materials, potentially inducing interfacial micro-annuli. In contrast, the K_1tg formation maintains stable shear strength, showing only a 2.63% decrease. Concerning caprock integrity, the J_1s formation presents a high risk of brittle failure, where the caprock is prone to sudden fracturing under pressure fluctuations. The enhanced plasticity of the J_1b formation reduces its fracture-closing capacity, lowering the CO_2 breakthrough pressure threshold by 15–20%. Although the K_1tg formation retains stable strength, stiffness loss still compromises its fracture resistance. The time-dependent mechanical degradation induced by CO_2–rock interaction is fundamentally a chemical–mechanical coupling process. The brittle deterioration of J_1s necessitates precautions against short-term wellbore integrity failure, while the plastic transformation of J_1b poses the greatest threat to the long-term sealing capacity of the caprock.

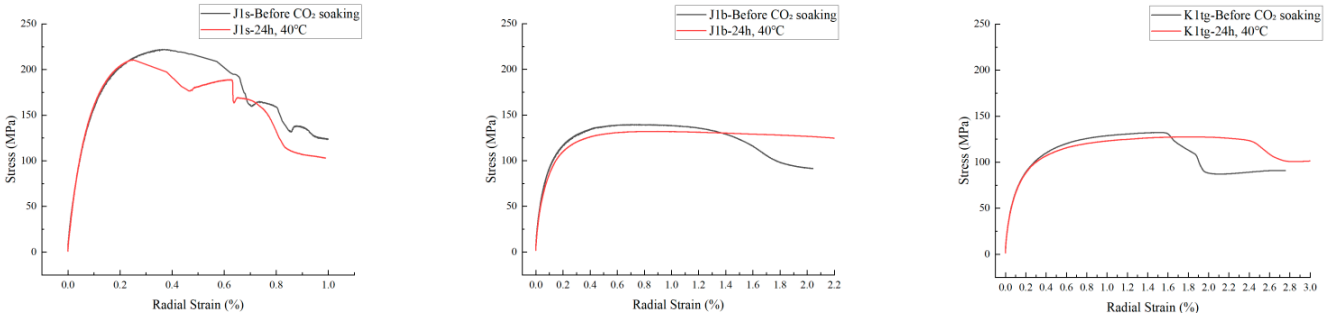

(**a**) J1s (**b**) J1b (**c**) K1tg

Figure 13. Stress–radial strain curve of different formations.

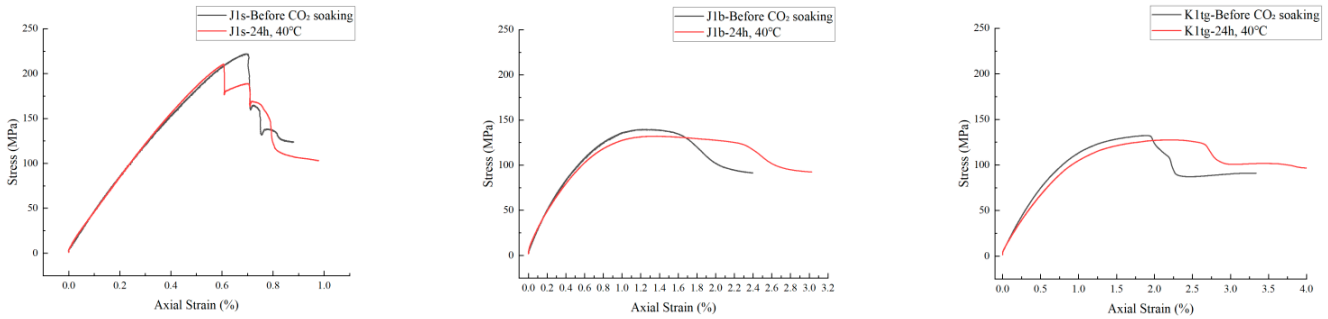

(**a**) J1s (**b**) J1b (**c**) K1tg

Figure 14. Stress–axial strain curve of different formations.

Figure 15 presents the load–strain curves of the J_1s, J_1b, and K_1tg formations obtained from uniaxial shear tests conducted after 24 h, 48 h, and 60 h of CO_2 immersion at 40 °C. The results indicate that with increasing CO_2 exposure time, the entire curves progressively shift toward the lower-load region, and the peak load values exhibit a consistent downward trend. This behavior reflects a gradual reduction in rock shear strength under prolonged CO_2 interaction. A strong positive correlation is observed between immersion duration and the extent of shear strength degradation, highlighting the continuous weakening effect of CO_2–brine–rock chemical interactions on the mechanical integrity of reservoir rocks.

These findings underscore the importance of considering time-dependent geochemical weakening in evaluating the long-term mechanical stability of CO_2 storage formations.

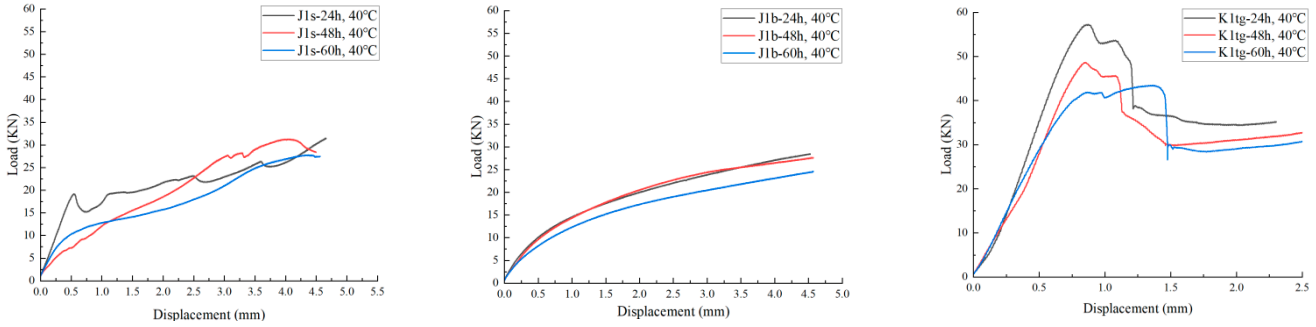

(**a**) J1s (**b**) J1b (**c**) K1tg

Figure 15. Load–displacement curves of 3 different formations.

4.3.1. Uniaxial Compressive Strength Test

Prior to immersion, the J_1s formation exhibited an elastic modulus of 37.778 GPa, a Poisson's ratio of 0.211, and a compressive strength of 222.173 MPa. After immersion at 40 °C for 24 h, the elastic modulus slightly increased to 38.296 GPa, Poisson's ratio decreased marginally to 0.206, and compressive strength declined to 210.608 MPa. Specifically, the compressive strength experienced a reduction of 11.565 MPa (a 5.20% decrease), the elastic modulus increased by 0.518 GPa (a 1.37% rise), and Poisson's ratio decreased by 0.005 (a 2.37% decline). These results indicate that immersion had a negligible impact on the elastic modulus and Poisson's ratio of the J_1s samples, suggesting stable elastic behavior and preserved structural rigidity. However, the notable decrease in compressive strength (5.2% reduction) implies that chemical interactions or physical degradation mechanisms induced by CO_2 exposure have compromised the rock's resistance to mechanical damage.

Prior to immersion, the K_1tg formation exhibited an elastic modulus of 11.714 GPa, a Poisson's ratio of 0.230, and a compressive strength of 127.643 MPa. After immersion at 40 °C for 24 h, the elastic modulus decreased to 10.500 GPa, Poisson's ratio declined to 0.218, and compressive strength reduced to 124.281 MPa. Specifically, the compressive strength decreased by 3.362 MPa (a 2.63% reduction), the elastic modulus declined by 1.214 GPa (a 10.36% reduction), and Poisson's ratio decreased by 0.012 (a 5.22% reduction). Despite the relatively pronounced reductions in the elastic modulus and Poisson's ratio, the modest decrease in compressive strength suggests that the K1tg formation maintains comparatively robust mechanical properties, retaining substantial structural integrity and resilience against external loading conditions.

4.3.2. Uniaxial Shear Resistance Test

After 24 h of immersion, the failure load of J_1s was 39.348 kN, decreasing to 31.256 kN after 48 h and 27.743 kN after 60 h. While the failure load decreases over time, the rate of change decays from 20.57% (8.092 kN) to 11.24% (3.513 kN), indicating that the mechanical properties of the formation degrade more drastically from 24 to 48 h, with the decline in failure load slowing over time. The most significant drop occurred from 24 to 48 h, with a decrease of 8.092 kN (20.57%), while the decline from 48 to 60 h slowed significantly to 3.513 kN (11.24%). This "fast–slow" decay trend suggests that the mechanical properties of J_1s rock samples are rapidly weakened in the early stage of CO_2 action, but the loss of structural stability slows as the reaction approaches saturation.

For J_1b, the failure load was 28.394 kN after 24 h of immersion, 27.595 kN after 48 h, and 24.573 kN after 60 h. The load decreased by 0.799 kN from 24 to 48 h and by 3.022 kN from 48 to 60 h, with the rate of change increasing from 2.81% to 10.95%—opposite to the

trend in J_1s. The failure load remained nearly stable from 24 to 48 h, decreasing by only 0.799 kN (2.81%), but dropped significantly by 3.022 kN (10.95%) from 48 to 60 h, indicating that degradation is minimal in the early stage but accelerates as the CO_2 immersion reaction progresses. This suggests that the J_1b formation may exhibit an illusion of apparent stability in the early stage of storage, but long-term stability risks increase, necessitating enhanced dynamic monitoring and pressure control in the post-injection phase.

For K_1tg, the failure load after 24 h CO_2 immersion was 57.303 kN, decreasing to 48.656 kN after 48 h and 43.555 kN after 60 h. The load reduction measured 8.647 kN (24 h→48 h) and 5.101 kN (48 h→60 h), with the degradation rate declining from 15.09% to 10.48%. In contrast, K_1tg formation exhibited an inverse trend: the failure load remained relatively stable during 24–48 h, with only a 0.799 kN reduction (2.81%), but showed significant deterioration of 3.022 kN (10.95%) during 48–60 h. This indicates negligible initial degradation but accelerated mechanical property attenuation as CO_2 dissolution reactions progressed. These results suggest that the K_1tg reservoir may demonstrate apparent short-term stability during early sequestration phases, while long-term stability risks increase substantially. Therefore, enhanced dynamic monitoring and pressure control during late-stage injection are recommended.

4.3.3. Geochemical Alterations Coupling with Geomechanical Properties

The J_1s formation manifests the preferential dissolution of silicate minerals, weakening the rock framework. Its high quartz content (56.9%) combined with plagioclase (24.1%) forms a rigid structure. Upon the CO_2 dissolution generating carbonic acid, plagioclase undergoes hydrolysis reactions, leading to dissolution at mineral contact points. The abrupt decline in intergranular cementation strength triggers microfracture propagation along quartz–feldspar interfaces. This is reflected in a 20.57% plummet in shear strength within 24 h, posing short-term risks of wellbore shear failure.

The J_1b formation exhibits clay mineral interlayer expansion and phase transformation, driving ductile transition. Swelling within clay mineral interlayers causes its Poisson's ratio to increase by 4.46% and elastic modulus to decrease by 11.27% after 48 h, promoting a brittle-to-ductile transformation. By 60 h, shear strength attenuation accelerates to 10.95%, resulting in a 15–20% reduction in a caprock breakthrough pressure threshold.

The K_1tg formation demonstrates suppressed structural damage through a dynamic carbonate dissolution–reprecipitation equilibrium. Calcite (42.6%) preferentially reacts with CO_2 to form soluble $Ca(HCO_3)_2$, while partial Ca^{2+} reprecipitates to seal pores. The low expansibility of illite–montmorillonite mixed-layer clay minimizes internal stress. Consequently, after 60 h of immersion, compressive strength declines by only 2.63%, shear strength attenuation stabilizes around 10%, and mechanical degradation remains the slowest.

5. Simulation Results

Numerical simulations are based on the Petrel geological models of the J_1b, J_1s, and K_1tg formations in the Baijiahai area, as shown in Figure 16a,b. The model spans 18,000 m horizontally, 14,000 m longitudinally, and 2600 m vertically. The Petrel geological models of the J_1b, J_1s, and K_1tg formations in the Baijiahai area were imported into the CMG numerical simulation software, and the initial physical property conditions of the models were set as shown in Figure 16c. To more intuitively observe the migration of injected CO_2 in the formation, the blocks shown in Figure 16d,e were selected for refinement. The selected area spans 1340 m in the I direction, 1340 m in the J direction, and 2600 m in the K direction. The Edit Grid function in Reservoir was used to refine the selected area, with the I and J directions refined 11 times and the K direction refined 7 times. The model has 33, 33,

and 66 grid cells in the I, J, and K directions, respectively, totaling 71,874 grids (excluding faults), as shown in Figure 16f.

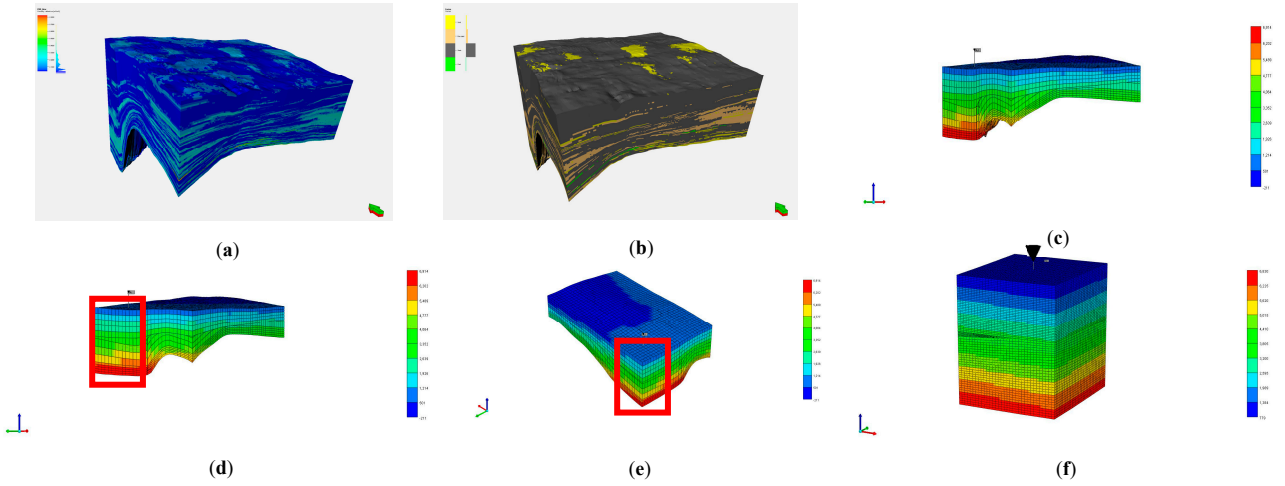

Figure 16. Petrel (**a**) porosity model, (**b**) sedimentary facies model, (**c**) CMG model in Petrel, (**d**,**e**) Location and Extent of the CMG Submodel, (**f**) The Refined CMG Submodel.

We added the experimental gas–water relative permeability curves for the three formations obtained from laboratory tests into CMG, as shown in Figure 17.

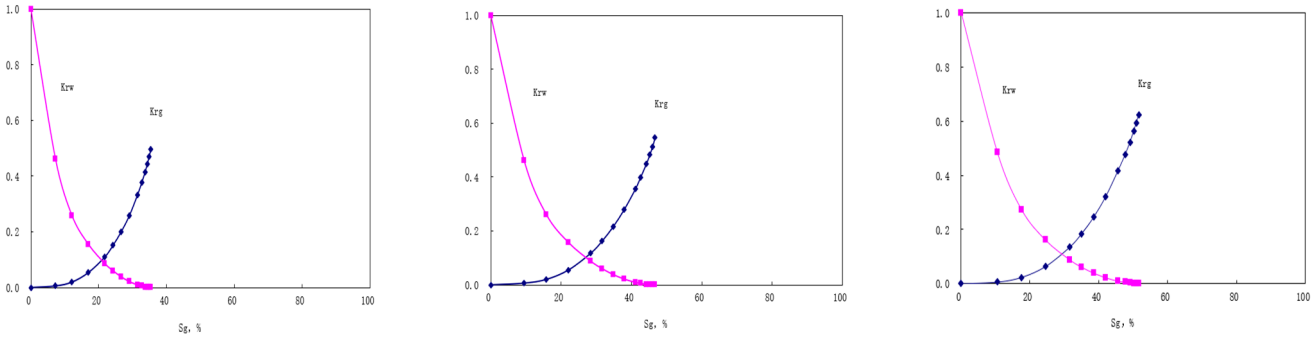

(**a**) K_1tg (**b**) J_1s (**c**) J_1b

Figure 17. Gas–water relative permeability curves for the three formations.

Taking the J_1b formation as an example, the J_1b core sample was utilized to establish an idealized model for the numerical simulation of the CO_2 flooding process with left-side injection and right-side production; configuring parameters according to Table 2, the gas–water relative permeability curves demonstrate that gas relative permeability reaches zero at a gas saturation of 51.65%, equivalent to a critical gas saturation of 51.65% in Figure 18. When these relative permeability curves were incorporated into the numerical simulation verification case, the resulting storage coefficient was approximately 54.9%. Compared with the 51.65% derived from the relative permeability curves in Figure 19, this represents a 93.98% consistency rate.

Table 2. Parameter configuration.

Length cm	Diameter cm	Porosity %	Permeability mD	Injection Pressure MPa	Outlet Pressure MPa	Temperature °C
5.208	2.514	26.559	13.140	11.6	11.5	40

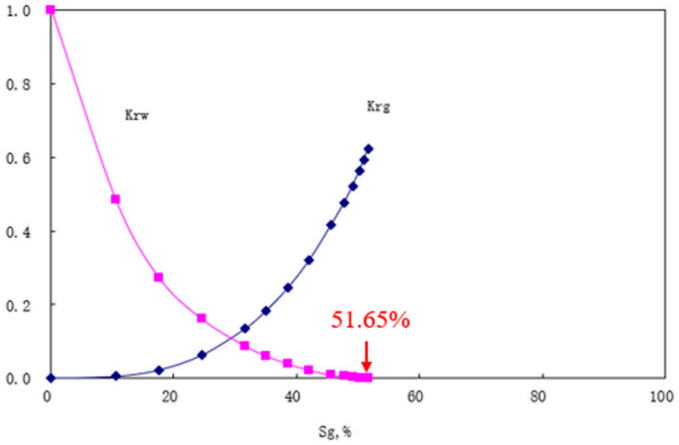

Figure 18. Gas–water relative permeability curves for the J_1b formation.

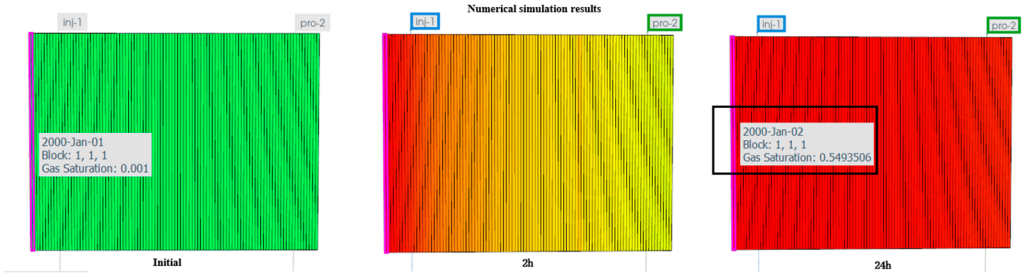

Figure 19. Displacement simulation results for the J_1b formation.

In the CCS module, the Land model was selected, and the maximum residual gas saturation calculated from the mercury intrusion test data in physical experiments was input into maximum residual gas saturation. After CO_2 enters the formation, it dissolves in water, generating CO_3^{2-} and HCO_{3-}, which react with formation rocks such as anorthite, kaolinite, and calcite. The following chemical equations were added to the mineralization reaction module in CCS:

$$CO_2 + H_2O \leftrightarrow H^+ + HCO_3^-$$

$$H^+ + OH \leftrightarrow H_2O$$

$$CO_3^{2-} + H^+ \leftrightarrow HCO_3^-$$

$$\text{Calcite } (CaCO_3) + H^+ \leftrightarrow Ca^{2+} + HCO_3^-$$

$$\text{Kaolinite } (Al_2Si_2O_5(OH)_4) + 6H^+ \leftrightarrow 5H_2O + 2SiO_2 + 2Al^{3+}$$

$$\text{Anorthite } (CaAl_2Si_2O_8) + 8H^+ \leftrightarrow 4H_2O + Ca^{2+} + 2SiO_2 + 2Al^{3+}$$

Injection wells are, respectively, set in the J_1s, J_1b, and K_1tg formations. The simulation conditions are as follows: the simulation time starts on 1 January 2000, with CO_2 injection lasting for 25 years. After the 25-year injection period, the wells are shut in, and the entire simulation continues for 100 years.

As shown in Figure 20a–i, the CO_2 migration in the K_1tg, J_1s, and J_1b formations is depicted at the initial state, after 25 years, and after 100 years. Upon CO_2 injection, the gas diffuses radially in the formation during the injection phase. After shutting in the injection wells, CO_2 primarily migrates vertically, with a greater migration volume in the vertical direction than in the horizontal direction, gradually forming a triangular shape.

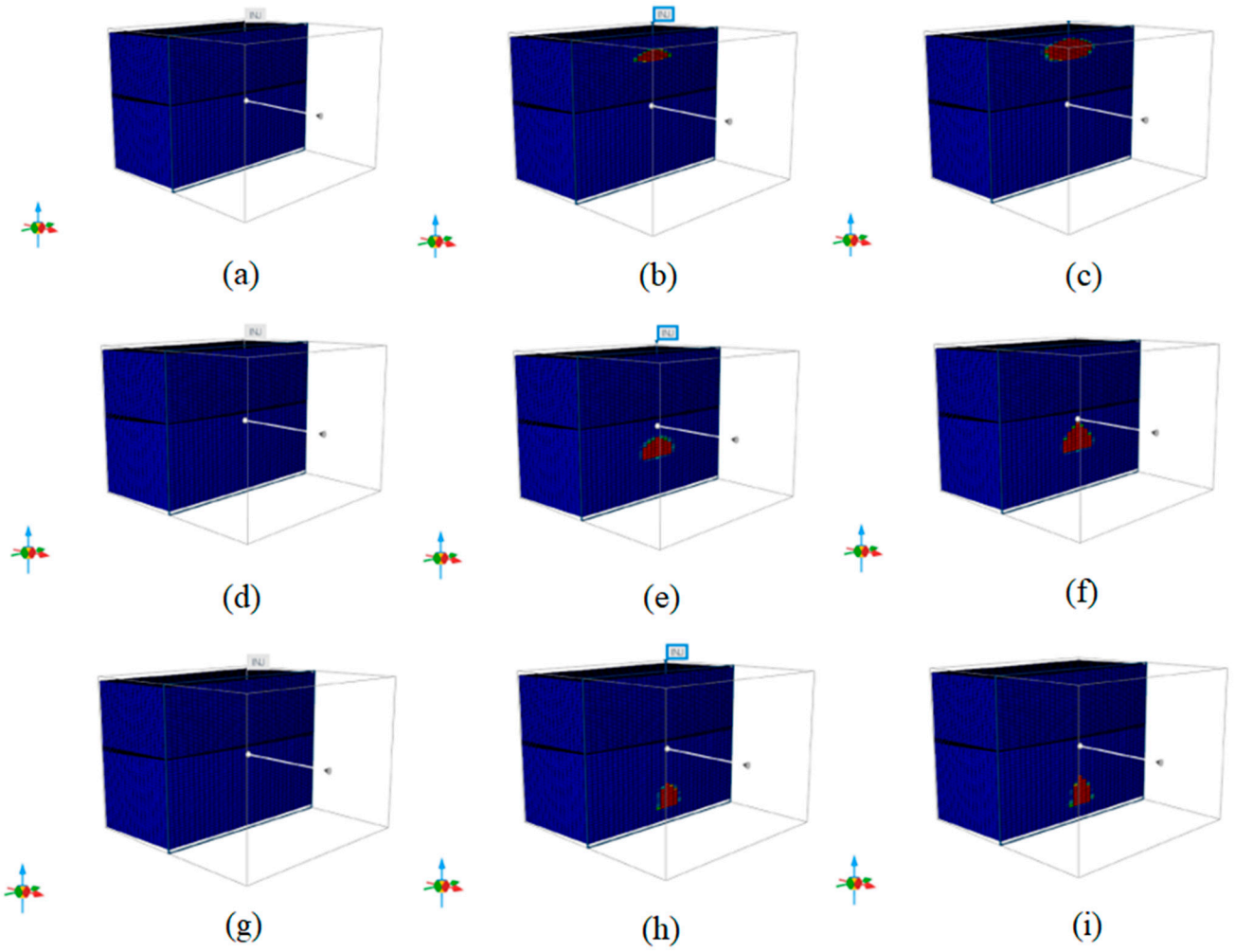

Figure 20. Initial state of 3 formations, and CO_2 migration patterns after 25 years and 100 years. (**a**) K_1tg formation initial state, (**b**) K_1tg formation CO_2 migration patterns after 25 years, (**c**) K_1tg formation CO_2 migration patterns after 100 years, (**d**) J_1s formation initial state, (**e**) J_1s formation CO_2 migration patterns after 25 years, (**f**) J_1s formation CO_2 migration patterns after 100 years, (**g**) J_1b formation initial state, (**h**) J_1b formation CO_2 migration patterns after 25 years, (**i**) J_1b formation CO_2 migration patterns after 100 years.

Figure 21a,b show that in the CO_2 aqueous phase, the CO_2 storage capacity of the K_1tg formation is higher than that of J_1s and J_1b. In the CO_2 dissolved phase, the storage capacities of all three formations gradually increase during CO_2 injection and plateaus after well shut-in, with J_1b ultimately exhibiting the highest storage capacity. As shown in Figure 21c, the K_1tg formation has the largest CO_2 storage capacity in the mineralized phase, but the differences among the three formations are minimal due to the extremely slow rate of mineralization. In the bound storage phase (Figure 21d), the storage capacities of all three formations increase before well shut-in, after which J_1b shows a more pronounced upward trend until it gradually stabilizes after 74 years. According to the numerical simulation results, the CO_2 storage capacities of the K_1tg, J_1s, and J_1b formations via different storage mechanisms after 100 years of simulation are summarized in Table 3, with the order of total storage capacity being J_1b > K_1tg > J_1s.

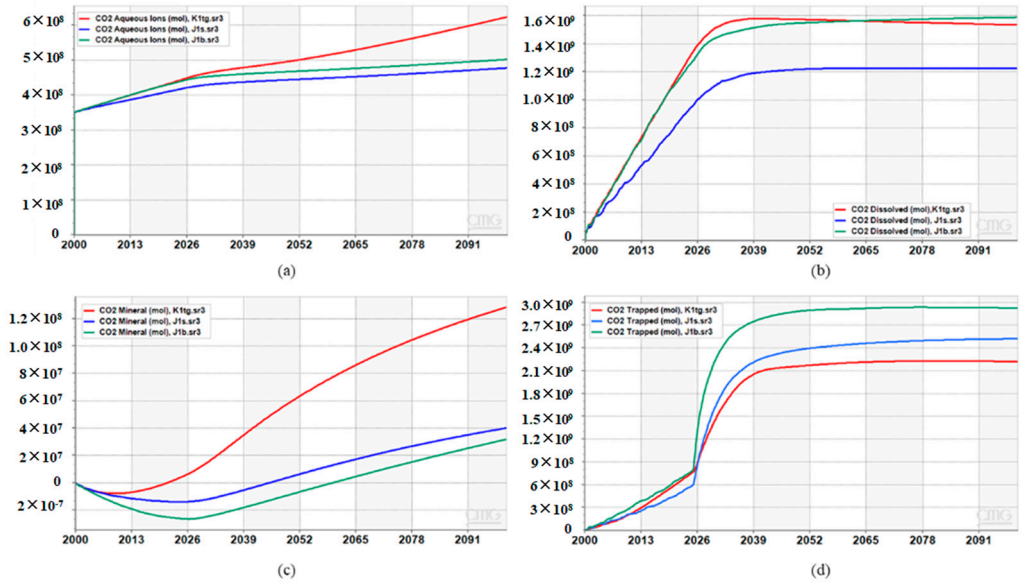

Figure 21. (**a**) Evolution of CO_2 storage capacity under CO_2 Aqueous Ions in 3 formations, (**b**) Evolution of CO_2 storage capacity under CO_2 Dissolved in 3 formations, (**c**) Evolution of CO_2 storage capacity under CO_2 Mineral in 3 formations, (**d**) Evolution of CO_2 storage capacity under CO_2 Trapped in 3 formations.

Table 3. CO_2 storage in 3 formations.

Stratum	CO_2 Aqueous (mol)	CO_2 Dissolved (mol)	CO_2 Mineral (mol)	CO_2 Super Critical (mol)	CO_2 Trapped (mol)	Total Storage Capacity (mol)
K_1tg	4.92821×10^8	1.49032×10^9	3.00589×10^7	2.65337×10^9	2.64899×10^9	4.666569×10^9
J_1b	4.97961×10^8	1.41702×10^9	4.50067×10^7	3.09315×10^9	3.06720×10^9	5.053138×10^9
J_1s	6.05990×10^8	1.41933×10^9	1.20637×10^8	2.12958×10^9	1.99623×10^9	4.275537×10^9

Porosity and permeability are two critical parameters influencing CO_2 geological storage. This study conducted a sensitivity analysis on the porosity and permeability of three formations: K_1tg, J_1s, and J_1b. The analysis applied parameter perturbations of $\pm 50\%$ and $\pm 20\%$ to each variable, with results quantified as deviations in cumulative CO_2 storage volume compared to baseline conditions.

$$\mathrm{Dev} = \frac{\mathrm{n} - \mathrm{nbase}}{\mathrm{nbase}} \quad (1)$$

The sensitivity analysis in Figure 22 demonstrates that for both the overall trend and individual formations, the parameters' impact on CO_2 storage capacity follows the order: porosity > permeability. Increasing either porosity or permeability enhances total CO_2 storage, though porosity exhibits more pronounced effects. These results suggest that strategically improving formation porosity (and to a lesser extent, permeability) can significantly increase CO_2 storage potential.

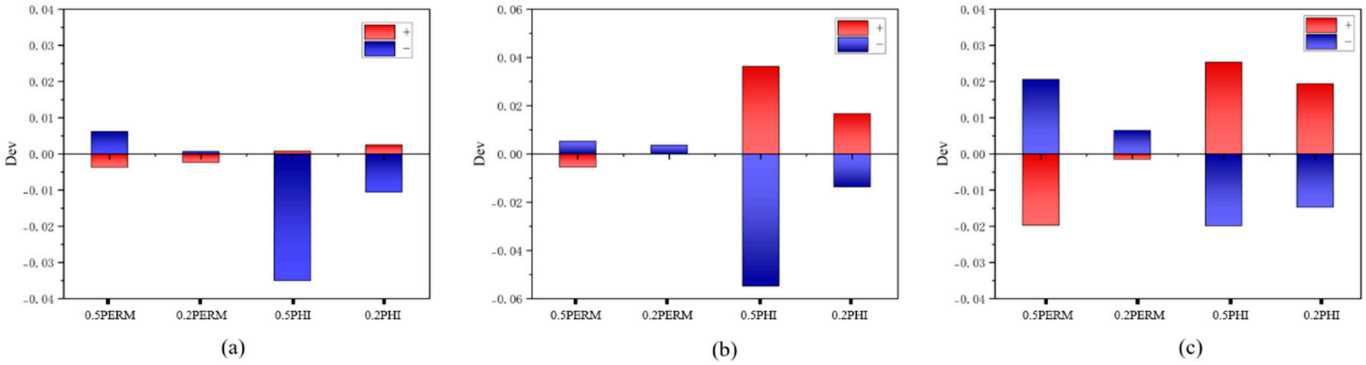

Figure 22. Sensitivity analysis of CO_2 storage parameters for (**a**) K_1tg, (**b**) J_1s, and (**c**) J_1b formations ("+" represents the deviation caused by increasing the parameters. "-" represents the deviation caused by increasing the parameters).

6. Discussions and Conclusions

This study focuses on three formations—J_1b, J_1s, and K_1tg—within the Baijiahai Uplift of the Junggar Basin. Through laboratory experiments (including CO_2 static immersion, dynamic displacement, NMR, and mercury injection capillary pressure [MICP] testing) and CMG numerical simulations, we systematically analyze physicochemical alterations, CO_2 storage mechanisms, and reservoir potential following CO_2 injection.

- The Jurassic Badaowan formation (J_1b) is characterized by high quartz content and kaolinite-dominated clay minerals, while the Jurassic Sangonghe formation (J_1s) consists mainly of quartz and plagioclase with lower and more diverse clay mineral content. The Cretaceous Tugulu Group (K_1tg) is rich in calcite and illite–smectite mixed-layer clays.
- Displacement experiments reveal sequestration efficiency rankings: J_1b(8.4%) > K_1tg(2.0%) > J_1s(1.2%). J_1b exhibits increased small pores and dominant large-pore sequestration; J_1s shows pore homogenization; K_1tg experiences preferential displacement in large pores with stable bound water in small pores. The superior capacity of J_1b is attributed to clay mineral (kaolinite) swelling and large-pore plugging effects.
- XRD and NMR analyses indicate that while J_1b has the smallest original pore-throat radius (median, 0.183 μm), it demonstrates the most comprehensive improvement in porosity and permeability after CO_2 immersion. J_1s achieves significant breakthroughs in permeability and a maximum pore-throat radius, whereas K_1tg forms a medium-pore preponderance due to calcite dissolution but with limited permeability enhancement.
- Mechanical tests show that J_1b has the highest sequestration potential but the poorest mechanical stability, requiring measures to prevent formation collapse. J_1s experiences a rapid 20% decline in shear strength within 24 h, necessitating injection pressure control during short-term operations.
- Numerical simulations confirm that J_1b achieves the highest total storage capacity through strong capillary trapping in clay minerals, despite weak mineralization. K_1tg ranks second due to calcite-driven mineralization and early aqueous storage, while J_1s performs mediocrely across all mechanisms.
- Optimal reservoir for CCUS: J_1b requires wellbore reinforcement technologies to address mechanical degradation.

Author Contributions: Methodology, Q.W.; investigation, S.Q.; writing—original draft, X.W.; writing—review and editing, W.Z.; visualization, K.W.; supervision, T.W. All authors have read and agreed to the published version of the manuscript.

Funding: This study has been supported by the China Petroleum Youth Science and Technology Project: Research on Geophysical Evaluation Methods for 10-Million-Ton Scale CCS Saline Aquifer Geological Storage Site Selection and Safety Monitoring (2024DQ03170), BGP Inc. Science and Technology Project: Integrated Technology Research for Carbon Dioxide Geological Storage Whole-Industry-Chain Demonstration Project (10-02-2025), BGP Inc. Science and Technology Project: Research on Underground Reservoir Evaluation and Monitoring Technology (10-02-2024). Science and Technology Development Program Project of the Silk Road Economic Belt Innovation-Driven Development Pilot Zone and the Urumqi-Changji-Shihezi National Independent Innovation Demonstration Zone: "Research on the Occurrence Mechanism and Key Development Technologies for Deep Coalbed Methane in Xinjiang" (2023LQ01005).

Data Availability Statement: The data were obtained from experiments and simulation results. The original contributions presented in this study are included in the article. Further inquiries can be directed to the corresponding authors.

Conflicts of Interest: Authors Xiaohui Wang, Wen Zhang, Qun Wang, Kepeng Wang and Saisai Qin were employed by the company BGP Inc., CNPC. The remaining author declares that the research was conducted in the absence of any commercial or financial relationships that could be construed as a potential conflict of interest.

References

1. Le Quéré, C.; Andrew, R.M.; Friedlingstein, P.; Sitch, S.; Hauck, J.; Pongratz, J.; Pickers, P.A.; Korsbakken, J.I.; Peters, G.P.; Canadell, J.G. Global carbon budget 2018. *Earth Syst. Sci. Data* **2018**, *10*, 2141–2194. [CrossRef]
2. Yoro, K.O.; Daramola, M.O. CO_2 emission sources, greenhouse gases, and the global warming effect. In *Advances in Carbon Capture*; Elsevier: Amsterdam, The Netherlands, 2020; pp. 3–28. [CrossRef]
3. Soeder, D.J. Greenhouse gas sources and mitigation strategies from a geosciences perspective. *Adv. Geo-Energy Res.* **2021**, *5*, 274–285. [CrossRef]
4. International Energy Agency (IEA). *Global CO_2 Emissions in 2023*; IEA: Paris, France, 2024. Available online: https://www.iea.org/reports/co2-emissions-in-2023 (accessed on 2 June 2025).
5. Dunn, R.J.H.; Aldred, F.; Gobron, N.; Miller, J.B.; Willett, K.M.; Ades, M.; Adler, R.; Allan, R.P.; Allan, R.; Anderson, J.; et al. Global climate. *Bull. Am. Meteorol. Soc.* **2021**, *102*, S11–S142. [CrossRef]
6. Khanal, A.; Shahriar, M.F. Optimization of CO_2 Huff-n-Puff in Unconventional Reservoirs with a Focus on Pore Confinement Effects, Fluid Types, and Completion Parameters. *Energies* **2023**, *16*, 2311. [CrossRef]
7. Zhan, J.; Niu, Z.; Li, M.; Zhang, Y.; Ma, X.; Fan, C.; Wang, R. Numerical simulation and modeling on CO_2 sequestration coupled with enhanced gas recovery in shale gas reservoirs. *Geofluids* **2021**, *2021*, 9975296. [CrossRef]
8. Shahriar, M.F.; Khanal, A. Fundamental investigation of reactive-convective transport: Implications for long-term carbon dioxide(CO_2) sequestration. *Int. J. Greenh. Gas Control.* **2023**, *127*, 103916. [CrossRef]
9. Yang, G.; Li, Y.; Ma, X.; Atrens, A.; Ni, H. Modeling study of enhanced thermal brine extraction using supercritical CO_2. *Bull. Geol. Sci. Technol.* **2014**, *33*, 233–240.
10. Li, Q.; Cai, B.; Chen, F.; Liu, G.; Liu, L. Review of environmental risk assessment methods for carbon dioxide geological storage. *Environ. Eng.* **2019**, *37*, 13–21.
11. Goodman, A.; Sanguinito, S.; Tkach, M.; Natesakhawat, S.; Kutchko, B.; Fazio, J.; Cvetic, P. Investigating the role of water on CO_2-utica shale interactions for carbon storage and shale gas extraction activities: Evidence for pore scale alterations. *Fuel* **2019**, *242*, 744–755. [CrossRef]
12. Cook, P.J. CCS research development and deployment in a clean energy future: Lessons from Australia over the past two decades. *Engineering* **2017**, *3*, 477–484. [CrossRef]
13. Jin, J.; Yang, G.; Liu, S.; Ma, X.; Zhang, Y.; Han, S. Effects of CO_2-saltwater-rock interaction on reservoir porosity: A case study of the Donggou Formation sandstone layer in the Junggar Basin. *Nonferrous Met. (Extr. Metall.)* **2025**, 204–216. Available online: https://link.oversea.cnki.net/doi/10.20237/j.issn.1007-7545.2025.02.023 (accessed on 2 June 2025).
14. Cai, B.; Li, Q.; Zhang, X.; Ouyang, T. *Annual Report of Carbon Dioxide Capture, Utilization and Storage (CCUS) in China (2021)—China CCUS Path Research*; Environmental Planning Institute of the Ministry of Ecology and Environment: Beijing, China, 2021.
15. Jafari, M.; Cao, S.C.; Jung, J. Geological CO_2 sequestration in saline aquifers: Implication on potential solutions of China's power sector. *Resour. Conserv. Recycl.* **2017**, *121*, 137–155. [CrossRef]
16. Vishal, V.; Singh, T. (Eds.) *Geologic Carbon Sequestration: Understanding Reservoir Behavior*; Springer: Cham, Switzerland, 2016; Volume 16, pp. 47–133.

17. Machado, M.V.B.; Delshad, M.; Sepehrnoori, K. Injectivity assessment for CCS field-scale projects with considerations of salt deposition, mineral dissolution, fines migration, hydrate formation, and non-Darcy flow. *Fuel* **2023**, *353*, 129148. [CrossRef]
18. Meguerdijian, S.; Pawar, R.J.; Harp, D.R.; Jha, B. Thermal and solubility effects on fault leakage during geologic carbon storage. *Int. J. Greenh. Gas Control.* **2022**, *116*, 103633. [CrossRef]
19. Li, Y. *Progress in Carbon Neutralization and Carbon Capture, Utilization and Storage Technology*; China Petrochemical Press Ltd.: Beijing, China, 2021. Available online: https://ricn.sjtu.edu.cn/Web/Show/77 (accessed on 2 June 2025).
20. Ye, H.; Hao, N.; Liu, Q. Review on Key Parameters and Characterization Technology of CO_2 Sequestration Mechanism in saline aquifers. *Power Gener. Technol.* **2022**, *43*, 562–573. [CrossRef]
21. Zhao, Y.; Yang, B.; Cao, C.; Zhang, L.; Zhou, X.; Huang, C.; Rui, Y.; Li, J. Research progress of evaluation of CO_2 storage potential and suitability assessment indexes in saline aquifers. *Pet. Reserv. Eval. Dev.* **2023**, *13*, 484–494.
22. Li, Y.; Pang, Z. Capacity and suitability assessment of deep saline aquifers for CO_2 sequestration in the Bohai Bay Basin, East China. *Environ. Earth Sci.* **2016**, *75*, 402. [CrossRef]
23. Gholami, R.; Raza, A. CO_2 sequestration in sandstone reservoirs: How does reactive flow alter trapping mechanisms. *Fuel* **2022**, *324*, 124781. [CrossRef]
24. Edem, D.; Abba, M.; Nourian, A.; Babaie, M.; Naeem, Z. Experimental investigation of the extent of the impact of Halite precipitation on CO_2 injection in deep saline aquifers. In Proceedings of the SPE Europec featured at EAGE Conference and Exhibition, SPE, Virtual, 1–3 December 2020. [CrossRef]
25. Haizheng, J.; Baiyang, L.; Zhao, L. Experimental study on the interaction between CO_2 and Jimsar reservoir rocks. *Chem. Eng. Oil Gas* **2021**, *50*, 76–80.
26. Amin, S.M.; Weiss, D.J.; Blunt, M.J. Reactive transport modelling of geologic CO_2 sequestration in saline aquifers: The influence of pure CO_2 and of mixtures of CO_2 with CH4 on the sealing capacity of cap rock at 37 °C and 100 bar. *Chem. Geol.* **2014**, *367*, 39–50. [CrossRef]
27. Alzayer, H.; Zahrani, T.; Shubbar, A. Modeling CO_2 Sequestration in Deep Saline Aquifers–Best Practices. In Proceedings of the International Petroleum Technology Conference, IPTC, Riyadh, Saudi Arabia, 21–23 February 2022. [CrossRef]
28. Youjun, J.; Xiaoyang, W.; Tiyao, Z.; Zegen, W.; Guobin, J. Effect of CO_2 geological sequestration on reservoir mechanical properties and gas migration and Diffusion Under Multi field coupling. *Environ. Eng.* **2023**, *41* (Suppl. S2), 442–446.
29. Zhou, Y.; Tang, L.; Song, Z.; Pan, B.; Yue, M.; Liu, J.; Song, H. Research on CO_2 sequestration in saline aquifers with different relative permeability considering CO_2 phase conditions. *Energy* **2024**, *313*, 133739. [CrossRef]
30. Peng, X.; Wang, Y.; Li, S.; Wang, X.; Cui, G.; He, Y. Migration characteristics and storage forms of liquid and supercritical CO_2 in saline aquifers. *Coal Geol. Explor.* **2025**, *53*, 99–106.
31. Fatima, S.; Khan, H.M.M.; Tariq, Z.; Abdalla, M.; Mahmoud, M. An experimental and simulation study of CO_2 sequestration in an underground formations; impact on geomechanical and petrophysical properties. In Proceedings of the SPE Middle East Oil and Gas Show and Conference, SPE, Event Canceled, 28 November–1 December 2021. [CrossRef]
32. Jin, Y.J.; Wang, J.L.; Pan, Z.Y. *Determination of CO_2 Solubility in Saline Solutions Under Geological Storage Conditions Using Raman Spectroscopy Combined with a Quartz Capillary Equilibrium Still*; Chinese Society for Mineralogy, Petrology and Geochemistry; Abstracts of the 17th Annual Conference of the Chinese Society for Mineralogy, Petrology and Geochemistry; College of Environmental Science and Engineering, Zhejiang University of Technology: Hangzhou, China, 2019; p. 1037.
33. Temitope, A.; Gomes, J.S.; Al Kobaisi, M.; Hu, J. Characterization and quantification of the CO_2 sequestration potential of a carbonate aquifer in Falaha Syncline, onshore Abu Dhabi. In Proceedings of the Abu Dhabi International Petroleum Exhibition & Conference, One Petro, Abu Dhabi, United Arab Emirates, 7–10 November 2016. [CrossRef]
34. Rezk, M.G.; Ibrahim, A.F. Impact of rock mineralogy on reactive transport of CO_2 during carbon sequestration in a saline aquifer. *J. Pet. Explor. Prod. Technol.* **2025**, *15*, 10. [CrossRef]
35. *GB/T 29172-2012*; Practices for Core Analysis. General Administration of Quality Supervision, Inspection and Quarantine of the People's Republic of China, Standardization Administration of the People's Republic of China: Beijing, China, 2012.

Disclaimer/Publisher's Note: The statements, opinions and data contained in all publications are solely those of the individual author(s) and contributor(s) and not of MDPI and/or the editor(s). MDPI and/or the editor(s) disclaim responsibility for any injury to people or property resulting from any ideas, methods, instructions or products referred to in the content.